Electronic Supplementary Material (ESI) for Nanoscale.

Influence of the support on stabilizing local defects in strained monolayer oxide films

Shuqiu Wang,[a] Xiao Hu,[a] Jacek Goniakowski,[b] Claudine Noguera,[b] and Martin R. Castell*[a]

[a] Department of Materials, University of Oxford, Parks Road, Oxford, OX1 3PH, U.K.

[b] CNRS-Sorbonne Université, UMR 7588, INSP, F-75005 Paris, France

* Email: martin.castell@materials.ox.ac.uk

Supporting Information

S1. Image processing procedures of multiple frame averaging.

Experimental STM images were processed using multiple frame averaging (MFA) to enhance the signal-to-noise ratio,[1] followed by smoothing using ImageJ, without using other image filtering.

The STM image in Fig. 1c was generated from 88 STM images. 88 raw images were taken from the same area, of the same image size, with no change in tip configuration and only minor changes in the STM image parameters. The 88 images were aligned to generate a stack of images sharing a common field of view. The process is called rigid alignment.[2] The resultant image stack was calculated into one averaged image which is called a reference image. Each raw image was

compared to the reference image so that drift, noise and distortions of the raw images could be corrected. This process is called non-rigid alignment.[2] 5 iterations of non-rigid alignment were performed to improve the signal-to-noise ratio, which finally produced an averaged image shown in Fig. 1c.

Fig. 4a was generated after averaging 4 frames. One raw STM image of the Stone-Wales (S-W) defect was taken. We used the known 2-fold symmetry of the S-W defect to rotate the image once by 180º and thereby doubled the number of the raw image to average. We also used the known mirror symmetry of the S-W defect to flip the 2 images and thereby doubled the number of raw images to average. This process produced 4 raw frames. The 4 frames were processed through 5 iterations of rigid alignment and 5 iterations of non-rigid alignment, which generated an averaged image. Finally, the averaged image was smoothed using ImageJ and shown in Fig. 4a.

Fig. 4b was generated after smoothing one raw STM image using ImageJ. The STM image cannot be manipulated using symmetry because there is a bright region to the left of the DV(5-8-5) structure and this region breaks the symmetry of the image.

Fig. 4c was generated after averaging 138 frames. 23 raw STM images of the DV(555-777) were taken from the same area, of the same image size, with no change in tip configuration or in the STM image parameters. We used the known 3-fold symmetry of the DV(555-777) defect to rotate the image twice by 120º and thereby tripled the number of raw images to average to 69 frames. We also used the known mirror symmetry of the DV(555-777) defect to flip the 69 images and thereby doubled the number of raw images to average. This process produced 138 raw frames. The 138 frames were processed through 5 iterations of rigid alignment and 5 iterations of non-rigid

alignment, which generated an averaged image. Finally, the averaged image was smoothed using ImageJ and shown in Fig. 4c.

Fig. 4d was generated after averaging 4 frames. One raw STM image of the DV(5555-6-7777) defect was taken. We used the known 2-fold symmetry of the DV(5555-6-7777) defect to rotate the image once by 180º and thereby doubled the number of the raw image to average. We also used the known mirror symmetry of the DV(5555-6-7777) defect to flip the 2 images and thereby doubled the number of raw images to average. This process produced 4 raw frames. The 4 frames were processed through 5 iterations of rigid alignment and 5 iterations of non-rigid alignment, which generated an averaged image. Finally, the averaged image was smoothed using ImageJ and shown in Fig. 4d.

Fig. 5 was generated from the same raw data and the same process as that for Fig. 4c, except that Fig. 5 was cropped from a larger field of view to show the strain field in the surrounding unit cells.

Fig. 6a was generated after averaging 12 frames. One raw STM image of the 'flower' defect was taken. We used the known 6-fold symmetry of the 'flower' defect to rotate the image once by 60º and thereby multiplied the number of the raw image to average by six. We also used the known mirror symmetry of the 'flower' defect to flip the 6 images and thereby doubled the number of raw images to average. This process produced 12 raw frames. The 12 frames were processed through 5 iterations of rigid alignment and 5 iterations of non-rigid alignment, which generated an averaged image. Finally, the averaged image was smoothed using ImageJ and shown in Fig. 6a.

S2. Computational methods and settings.

S2a. Reference calculations on the pristine supported oxide film were performed in a small (1 × 1)- Ti_2O_3 (111) // (2 × 2)-Au(111) coincidence cell, with the Ti_2O_3 film deposited on one side of the Au(111) slab composed of four atomic Au layers. Periodic slab images were separated by more than 10 Å of vacuum, and dipole corrections were used to eliminate the remaining spurious interactions between periodic replicas. The in-plane lattice parameters were fixed at the experimental gold lattice parameter of 4.08 Å and the reciprocal space was sampled with a fine (14 × 14 × 1) Monkhorst-Pack grid. Atomic positions of all ions in the Ti_2O_3 film were fully optimized, while those of Au atoms were relaxed only in the direction normal to the surface (threshold on forces = 0.01 eV/Å). We found that using a thicker slab (6 Au layers) improves the film atomic structure (adsorption height, film rumpling) by less than 0.01 Å, the interaction strength (separation energy) by less than 0.03 eV/Ti_2O_3, and interface charge transfer by only about 0.02 e^-/Ti_2O_3. Interestingly, a refinement of the oxide electronic structure within the DFT+U approximation[3] (U-J = 3 eV) and an account for the dispersion forces[4,5] have only a similarly small impact on the film structure (the adsorption height is shortened by 0.01 Å and the film rumpling is increased by 0.03 Å), despite a non-negligible reinforcement of its interaction strength with the gold substrate (the separation energy increases by 0.6 eV/Ti_2O_3) and of the interface charge transfer (by 0.1 e^-/Ti_2O_3).

S2b. Large-cell models. In order to attenuate the in-plane interaction between periodic images, we used a large (√21 × √21)R11° - Ti_2O_3 (111) // (2√21 × 2√21)R11° -Au(111) surface unit cell for the defect calculations. In these calculations standard titanium and gold, and soft oxygen (energy cutoff of 270 eV) pseudo-potentials provided by VASP were used, enabling a thorough structural relaxation of all the systems that were studied. Results on the perfect supported

honeycomb film obtained with the soft and the full (energy cutoff of 400 eV) oxygen pseudo-potentials were analyzed and showed that differences of structural characteristics (adsorption height, film rumpling) were below 0.01 Å, that the oxide/metal separation energies were smaller than 0.02 eV/Ti_2O_3, and that interface charge transfer changed by less than 0.03 e^-/Ti_2O_3 only. Moreover, in the large cell calculations, only three Au(111) atomic layers were used to represent the gold substrate and the reciprocal space was sampled with a single Gamma point. While the resulting structure of the supported film and the interface charge transfer obtained with these settings differ by similarly small amounts from the reference results, the separation energy is increased by about 0.3 eV/Ti_2O_3.

S2c. The oxide-metal interaction strength was estimated by the separation energy, E_{sep} = [$E(Ti_2O_3/Au) - E(Ti_2O_3) - E(Au)$], where $E(Ti_2O_3/Au)$, $E(Ti_2O_3)$, and E(Au) are the total energies of the oxide-covered slab, of an unsupported relaxed oxide layer (with the same in-plane lattice parameters as in the supported one), and of the gold slab, respectively. We note that an additional 0.8 eV/Ti_2O_3 is released when the in-plane lattice parameter of the unsupported honeycomb film is optimized.

S2d. Defect formation energies. In the *supported* case, defect formation energies were evaluated with respect to the pristine supported honeycomb film, $E_{form} = E(Ti_2O_3+defect/Au) - E(Ti_2O_3/Au) + n/m[E(Ti_2O_3/Au) - E(Au)]$, where $E(Ti_2O_3+defect/Au)$ and $E(Ti_2O_3/Au)$ are the total energies of the defective and pristine supported honeycomb films, respectively, and the factor n/m accounts for the Ti_2O_3 deficiency in the defective film (n =1 formula unit in all considered cases, except for the Stone-Wales defect for which n = 0), with respect to the number of Ti_2O_3 formula units in the surface unit cell (m = 24). In the *unsupported* case, E_{form} (free) = $E(Ti_2O_3+defect) - E(Ti_2O_3)$ +

n/m E(Ti_2O_3), where E(Ti_2O_3+defect) and E(Ti_2O_3) are the total energies of the unit cell of defective and pristine honeycomb films, respectively.

S2e. Elastic energies of the defective films were estimated for the film structures obtained from full optimization at the ab initio level, by applying the standard expression of elastic bond energy as a function of bond length d: $E(d) = k(d - d_0)^2$ to all Ti-O bonds in the unit cell. The bond equilibrium length d_0 = 1.84/1.82 Å (unsupported/supported) and the elastic coefficient k ~ 20 eV/Å^2 were obtained by fitting to ab initio results on uniformly distorted (stretched/compressed) pristine Ti_2O_3 films.

S2f. The intrinsic lattice parameter of the Au-supported Ti_2O_3 film, a_0, was estimated from the minimum of energy difference E(Ti_2O_3/Au)(a) – E(Au)(a) as a function of the lattice parameter a. E(Ti_2O_3/Au)(a) and E(Au)(a) are the total energies of the Ti_2O_3–covered and bare Au slabs, respectively, both calculated for the same value of the in-plane lattice parameter a.

S3. Details of computational results.

Table S1 summarizes the calculated structural and electronic characteristics of the four defects under consideration.

	S-W	DV(5-8-5)	DV(555-777)	DV(5555-6-7777)
δd_{Ti-O} (Å)	0.02	0.05	0.05	0.05
$\delta< z_{Ti} >$ (Å)	0.03	0.09	0.16	0.08
δr_{Ti-O} (Å)	-0.06	-0.15	-0.18	-0.13
$\delta\|q_{Au}\|$ (e)	-0.2	-1.8	-1.8	-1.9
$\delta\Phi$ (eV)	-0.2	-0.3	-0.3	-0.3

Table 1**.** Calculated changes of film structural and electronic characteristics at the defect cores with respect to the pristine Ti_2O_3 structure: maximal expansion of the Ti-O bond lengths δd_{Ti-O} (Å), average elevation of the Ti atoms $\delta< z_{Ti} >$ (Å), minimal value of the film rumpling δr_{Ti-O} (Å), electron transfer towards Au $\delta|q_{Au}|$ (e), and defect-induced change of surface work function $\delta\Phi$ (eV).

S4. Generation of a Ti_2O_3 divacancy defect during STM imaging.

The formation of Ti_2O_3 divacancy defects via tip-surface interactions were sometimes observed during STM imaging. Fig. S1a shows a STM image of the pristine honeycomb surface. In the subsequent scan (Fig. S1b), a DV(5555-6-7777) defect and a S-W defect appear on the left part of the image. A Ti_2O_3 cluster is removed by the STM tip followed by rearrangement of the honeycomb lattice into pentagons and heptagons.

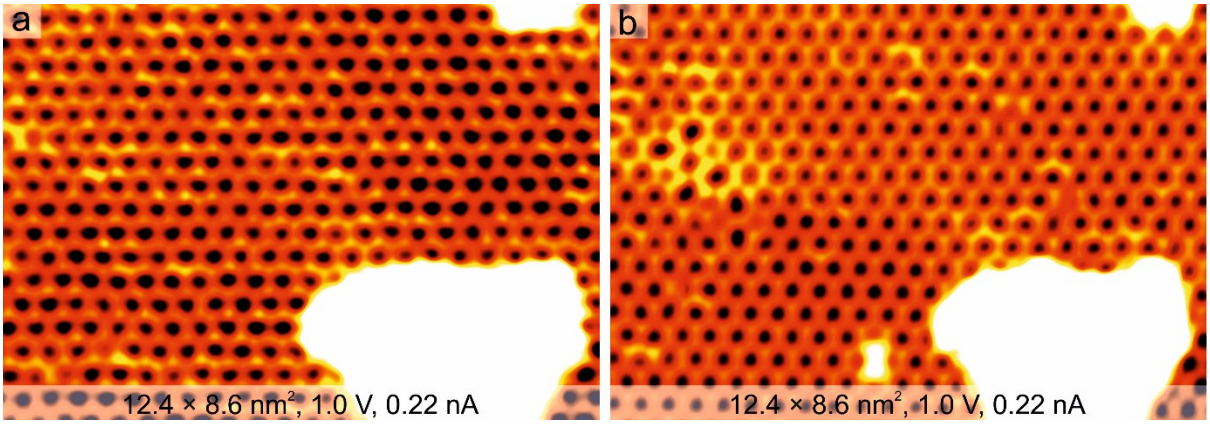

Fig. S1 The formation of divacancy defects in Ti_2O_3-Au(111). Consecutive STM images showing (a) the pristine honeycomb film, and (b) the appearance of a DV(5555-6-7777) defect and a S-W defect.

References & notes

1 L. Jones, S. Wang, X. Hu, S. ur Rahman and M. R. Castell, *Adv. Struct. Chem. Imaging*, 2018, **4**, 7.

2 L. Jones, H. Yang, T. J. Pennycook, M. S. J. Marshall, S. Van Aert, N. D. Browning, M. R. Castell and P. D. Nellist, *Adv. Struct. Chem. Imaging*, 2015, **1**, 8.

3 S. L. Dudarev, G. A. Botton, S. Y. Savrasov, C. J. Humphreys and A. P. Sutton, *Phys.*

Rev. B, 1998, **57**, 1505.

4 J. Klimeš, D. R. Bowler and A. Michaelides, *J. Phys.: Condens. Matter*, 2010, **22**, 022201.

5 J. Klimeš, D. R. Bowler and A. Michaelides, *Phys. Rev. B*, 2011, **83**, 195131.